The Astrophysical Journal, 952:84 (15pp), 2023 July 20 https://doi.org/10.3847/1538-4357/acd643

The GLASS-JWST Early Release Science Program. III. Strong-lensing Model of Abell 2744 and Its Infalling Regions

Pietro Bergamini[1,2], Ana Acebron[1,3], Claudio Grillo[1,3], Piero Rosati[2,4], Gabriel Bartosch Caminha[5,6], Amata Mercurio[7,8], Eros Vanzella[2], Charlotte Mason[9,10], Tommaso Treu[11], Giuseppe Angora[4,8], Gabriel B. Brammer[9,10], Massimo Meneghetti[2,12], Mario Nonino[13], Kristan Boyett[14,15], Maruša Bradač[16,17], Marco Castellano[18], Adriano Fontana[18], Takahiro Morishita[19], Diego Paris[18], Gonzalo Prieto-Lyon[9,10], Guido Roberts-Borsani[11], Namrata Roy[20], Paola Santini[18], Benedetta Vulcani[21], Xin Wang[22,23,24], and Lilan Yang[25]
[1] Dipartimento di Fisica, Università degli Studi di Milano, Via Celoria 16, I-20133 Milano, Italy; pietro.bergamini@unimi.it
[2] INAF—OAS, Osservatorio di Astrofisica e Scienza dello Spazio di Bologna, via Gobetti 93/3, I-40129 Bologna, Italy
[3] INAF—IASF Milano, via A. Corti 12, I-20133 Milano, Italy
[4] Dipartimento di Fisica e Scienze della Terra, Università degli Studi di Ferrara, via Saragat 1, I-44122 Ferrara, Italy
[5] Physik-Department, Technische Universität München, James-Franck Str. 1, D-85741 Garching, Germany
[6] Max-Planck-Institut für Astrophysik, Karl-Schwarzschild-Str. 1, D-85748 Garching, Germany
[7] Dipartimento di Fisica "E.R. Caianiello," Università Degli Studi di Salerno, Via Giovanni Paolo II, I-84084 Fisciano (SA), Italy
[8] INAF—Osservatorio Astronomico di Capodimonte, Via Moiariello 16, I-80131 Napoli, Italy
[9] Cosmic Dawn Center (DAWN), Jagtvej 128, DK-2200 Copenhagen N, Denmark
[10] Niels Bohr Institute, University of Copenhagen, Jagtvej 128, København N, DK-2200, Denmark
[11] Department of Physics and Astronomy, University of California, Los Angeles, 430 Portola Plaza, Los Angeles, CA 90095, USA
[12] National Institute for Nuclear Physics, viale Berti Pichat 6/2, I-40127 Bologna, Italy
[13] INAF—Osservatorio Astronomico di Trieste, via G.B. Tiepolo 11, I-34131 Trieste, Italy
[14] School of Physics, University of Melbourne, Parkville, VIC 3010, Australia
[15] ARC Centre of Excellence for All Sky Astrophysics in 3 Dimensions (ASTRO 3D), Australia
[16] Department of Mathematics and Physics, University of Ljubljana, Jadranska ulica 19, SI-1000 Ljubljana, Slovenia
[17] Department of Physics and Astronomy, University of California Davis, 1 Shields Avenue, Davis, CA 95616, USA
[18] INAF—Osservatorio Astronomico di Roma, Via Frascati 33, I-00078 Monteporzio Catone, Rome, Italy
[19] IPAC, California Institute of Technology, MC 314-6, 1200 E. California Boulevard, Pasadena, CA 91125, USA
[20] Center for Astrophysical Sciences, Department of Physics & Astronomy, Johns Hopkins University, Baltimore, MD 21218, USA
[21] INAF—Osservatorio astronomico di Padova, Vicolo Osservatorio 5, I-35122 Padova, Italy
[22] School of Astronomy and Space Science, University of Chinese Academy of Sciences (UCAS), Beijing 100049, People's Republic of China
[23] National Astronomical Observatories, Chinese Academy of Sciences, Beijing 100101, People's Republic of China
[24] Institute for Frontiers in Astronomy and Astrophysics, Beijing Normal University, Beijing 102206, People's Republic of China
[25] Kavli Institute for the Physics and Mathematics of the Universe, The University of Tokyo, Kashiwa, 277-8583, Japan
Received 2023 March 17; revised 2023 April 21; accepted 2023 May 3; published 2023 July 21

Abstract

We present a new high-precision, JWST-based, strong-lensing model for the galaxy cluster Abell 2744 at $z = 0.3072$. By combining the deep, high-resolution JWST imaging from the Grism Lens Amplified Survey from Space–JWST and Ultradeep NIRSpec and NIRCam Observations before the Epoch of Reionization programs and a Director's Discretionary Time program, with newly obtained Very Large Telescope/Multi Unit Spectroscopic Explorer (MUSE) data, we identify 32 multiple images from 11 background sources lensed by two external subclusters at distances of $\sim 160''$ from the main cluster. The new MUSE observations enable the first spectroscopic confirmation of a multiple-image system in the external clumps. Moreover, the reanalysis of the spectrophotometric archival and JWST data yields 27 additional multiple images in the main cluster. The new lens model is constrained by 149 multiple images ($\sim$66% more than in our previous model) covering an extended redshift range between 1.03 and 9.76. The subhalo mass component of the cluster includes 177 member galaxies down to $m_{\rm F160W} = 21$, of which 163 are spectroscopically confirmed. Internal velocity dispersions are measured for 85 members. The new lens model is characterized by a remarkably low scatter between the predicted and observed positions of the multiple images ($0\farcs43$). This precision is unprecedented given the large multiple-image sample, the complexity of the cluster mass distribution, and the large modeled area. The improved precision and resolution of the cluster total mass distribution provides a robust magnification map over a $\sim$30 arcmin^2 area, which is critical for inferring the intrinsic physical properties of the highly magnified, high-z sources. The lens model and the new MUSE redshift catalog are released with this publication.

Unified Astronomy Thesaurus concepts: Galaxy clusters (584); Strong gravitational lensing (1643); Dark matter (353)

Supporting material: machine-readable tables

1. Introduction

The first JWST observations of massive galaxy clusters have revealed exceptionally rich background patterns of strongly lensed galaxies, thanks to a revolutionary combination of

angular resolution, depth and near-and mid-infrared coverage (e.g., Caminha et al. 2022; Pascale et al. 2022; Mahler et al. 2023). Several JWST survey programs have targeted cluster fields to exploit the gravitational lensing magnification, in the effort to unveil primordial star-forming systems and study their physical properties (e.g., Bezanson et al. 2022; Treu et al. 2022; Willott et al. 2022; Windhorst et al. 2023). While current studies are identifying an increasing number of strongly lensed sources at $z \gtrsim 8$ based on JWST Near Infrared Camera (NIRCam) photometry (Bradley et al. 2022; Hsiao & Coe 2023; Adams et al. 2023), some have already obtained spectroscopic confirmations in the range $z = 9.5$–10 (Roberts-Borsani et al. 2022; Williams et al. 2023).

Compared to blank field surveys, observations of highly magnified regions of clusters have the advantage of extending to low luminosities and stellar masses our knowledge of the galaxy populations in the first billion years of cosmic history, providing unique insights on their inner structure down to parsec resolutions (e.g., Bouwens et al. 2021; Meštrić et al. 2022; Vanzella et al. 2022, 2023; Welch et al. 2023). This progress, however, comes with significant challenges. High-precision strong-lensing models are needed to produce reliable magnification maps, which are, in turn, critical to infer the intrinsic physical properties of the lensed sources (luminosities, stellar masses, star formation rates, sizes), as well as the effective survey volume at varying redshifts and therefore their space densities (Castellano et al. 2022). The accuracy and precision of lens models in predicting accurate magnification (μ) values depend essentially on the number of bona-fide multiple images with spectroscopic redshifts, spanning a wide z range, and a complete knowledge of the member galaxies contributing to the cluster mass distribution. While independent models based on high-quality spectrophotometric data tend to be robust in the low-magnification regime ($\mu \lesssim 3$; see, e.g., Meneghetti et al. 2017; Priewe et al. 2017), such a requirement becomes progressively more important near the critical lines, at $\mu \gtrsim 10$. In the most extreme cases, for sources found within a fraction of arcseconds of a critical line (e.g., Chen et al. 2022; Diego et al. 2022; Welch et al. 2022; Meena et al. 2023), including caustic crossing events (Kelly et al. 2018), magnification values can be on the order of hundreds or more, implying that the interpretation on the nature of the source relies heavily on the lens model accuracy.

JWST observations of galaxy clusters with exceptional lensing cross sections offer an unprecedented opportunity to zoom into primordial star-forming regions. On the one hand, they also provide a high number density of multiple-image systems, a factor of 2–3 higher than Hubble Space Telescope (HST)-based studies, which improves the accuracy of the lens models. On the other hand, spectroscopic redshifts of a significant fraction of these lensed sources, which were beyond the reach of previous technology, have now become attainable with JWST.

In this context, the massive galaxy cluster Abell 2744 (hereafter A2744), at $z = 0.3072$, has been the target of several observational campaigns with the HST obtaining deep, high-resolution, and wide-field coverage (Lotz et al. 2017; Steinhardt et al. 2020). Its combination with extensive ground- and space-based spectroscopic follow-up observations (Braglia et al. 2009; Owers et al. 2011; Treu et al. 2015; Richard et al. 2021) has enabled a new generation of strong-lensing models including a large number of secure multiple images (Wang et al. 2015; Richard et al. 2021; Bergamini et al. 2023a, hereafter B23). In particular, the lens model presented by B23 prior to the JWST observations included 90 spectroscopically confirmed multiple images (from 30 background sources), achieving an accuracy in reproducing the observed positions of the multiple images of a factor of 2 better than those of previous lens models (see, e.g., Wang et al. 2015; Mahler et al. 2018; Richard et al. 2021). These pre-JWST lens models found that several massive structures residing at large distances from the main cluster core had a nonnegligible impact on the total mass reconstruction of the cluster inner regions. B23 found magnification to be significantly different from one well beyond the innermost 500 kpc from the cluster center, suggesting that these specific regions cannot effectively be considered as blank fields.

More recently, A2744 has been among the first targets of JWST (Bezanson et al. 2022; Treu et al. 2022). By exploiting the deep JWST/NIRCam observations gathered from both programs, Furtak et al. (2023, hereafter F23) presented a lens model, identifying, for the first time, a large number of photometric multiple images around the external clumps. The F23 lens model (optimized on the source plane) is constrained by the observed positions of 135 multiple images (from 47 background sources), and it is characterized by an rms residual scatter on the lens plane of $0\farcs66$ in the multiple-image positions, compared to $0\farcs37$ for the model by B23.

In this work, we exploit the new JWST/NIRCam imaging and Multi Unit Spectroscopic Explorer (MUSE) spectroscopic observations, together with archival spectrophotometric data including recent JWST Near Infrared Imager and Slitless Spectrograph (NIRISS) and JWST Near Infrared Spectrograph (NIRSpec) redshifts, to build an improved lens model of A2744 that includes the largest sample of multiple images used to date. In addition, the new identification of several multiple-image systems in the cluster core and around the external clumps enables a more accurate and precise reconstruction of the total mass distribution of the cluster. The lens model presented in this work plays a fundamental role in studying the intrinsic properties of the lensed high-redshift sources from current and future JWST observations of A2744.

The paper is organized as follows. Section 2 describes the archival imaging and spectroscopic data sets, as well as the new JWST and MUSE observations, which are used to develop the lens model of A2744. In Section 3, we detail the selection of the multiple images and cluster members, and the adopted methodology for the extended strong-lensing modeling of the cluster. Our results are discussed in Section 4, and our main conclusions are summarized in Section 5.

Throughout this work, we adopt a flat Lambda cold dark matter (ΛCDM) cosmology with $\Omega_m = 0.3$ and $H_0 = 70\,\mathrm{km\,s^{-1}\,Mpc^{-1}}$. Using this cosmology, a projected distance of $1''$ corresponds to a physical scale of 4.528 kpc at the A2744 redshift of $z = 0.3072$. All magnitudes are given in the AB system.

2. Data

This section presents the data sets used to build the extended strong-lensing model of A2744, focusing in particular on the new spectrophotometric data compared to those exploited by B23. In Section 2.1, we describe the archival HST and Magellan imaging as well as the new JWST NIRCam imaging of this cluster field. Section 2.2 summarizes the spectroscopic

coverage of the cluster field and the new MUSE Director's Discretionary Time (DDT) observations.

2.1. Imaging Data

We use deep, ancillary Magellan *g, r, i* imaging of A2744 obtained with MegaCam on the Magellan 2 Clay Telescope on 2018 September 7–8 (see Treu et al. 2022 for an overview). The Magellan *i*-band imaging was used to anchor the NIRCam images to the Gaia Data Release 3 (DR3) astrometric solution (see Paris et al. 2023). All the coordinates in our new lens model are therefore also aligned to this World Coordinate System (WCS).[26] The uniform Magellan multiband photometry over the entire field can also be used to check the color consistency of a few cluster members lying outside the HST coverage.

In addition, A2744 is one of the cluster fields with the deepest high-resolution observations obtained with HST thanks to the Hubble Frontier Fields program[27] (HFF; Proposal ID: 13495; Lotz et al. 2017) and other ancillary data from previous HST observational campaigns. The Beyond Ultra-deep Frontier Fields And Legacy Observations (BUFFALO; Steinhardt et al. 2020) survey has since provided an extended but shallower coverage of the cluster field. In this work, we make use of the HFF and BUFFALO HST mosaics that are described by B23.

Finally, we exploit the new JWST NIRCam imaging of A2744 obtained within the Grism Lens Amplified Survey from Space (GLASS)-JWST program Early Release Science (ERS)-1324 (PI: Treu; Treu et al. 2022), the Ultradeep NIRSpec and NIRCam ObserVations before the Epoch of Reionization (UNCOVER) Cycle 1 Treasury program (GO-2561, PIs: Labbé and Bezanson; Bezanson et al. 2022), and the DDT program 2756 (PI: Chen). The footprints from these three observational programs are shown in Figure 1 in orange, blue, and red, respectively. The fields of view, the filters, and the data reduction are detailed in Merlin et al. (2022) and Paris et al. (2023). Briefly, the resulting JWST/NIRCam coverage of the cluster from the three programs includes observations with eight different filters (F090W, F115W, F150W, F200W, F277W, F356W, F410M, F444W), over an area of 46.5 arcmin^2 with a $0\farcs031$ pixel scale. The final 5σ magnitude limit of the images ranges from ∼28.6 AB to ∼30.2 AB, depending on the location and filters. The reduced NIRCam images and the associated multiwavelength catalogs are made publicly available (doi:10.17909/kw3c-n857).[28] The photometric redshifts are computed by means of the spectral energy distribution (SED) fitting code zphot.exe (Fontana et al. 2000). Using the same method and assumptions as in Merlin et al. (2021) and Santini et al. (2023), we have built the stellar library by adopting the Bruzual & Charlot (2003) models and including nebular emission lines according to Castellano et al. (2014) and Schaerer & de Barros (2009).

2.2. Spectroscopic Data

The A2744 cluster field counts with an extensive spectroscopic coverage obtained with several ground and space-based facilities; see B23 for a detailed overview. Briefly, A2744 was observed with the wide-field VIsible Multi-Object Spectrograph (VIMOS) as part of the ESO Large Program 169.A-0595 (PI: Böhringer; Braglia et al. 2009), the AAOmega multiobject spectrograph on the 3.9 m Anglo-Australian Telescope (Owers et al. 2011), and the HST Wide Field Camera 3/IR grism through the HST GO program GLASS[29] (Schmidt et al. 2014; Treu et al. 2015). The ∼4 arcmin^2 central region of the galaxy cluster (green footprints in Figure 1) was then targeted with the MUSE integral field spectrograph, mounted on the Very Large Telescope (VLT; Bacon et al. 2012), within the GTO Program 094.A-0115 (PI: Richard). The data consist of five MUSE pointings, each with total exposure times raging from 2 to 5 hr (Mahler et al. 2018; Richard et al. 2021; B23), allowing for the spectroscopic confirmation of a large number of multiple-image systems and cluster members.

Besides these archival data, additional VLT/MUSE spectroscopy within the GLASS-JWST NIRCam fields was recently acquired through the ESO DDT program 109.24EZ.001 (PIs: Mason, Vanzella) on the nights of 2022 July 28 and 2022 August 20 (see also Prieto-Lyon et al. 2023 for further details). The new data comprise five pointings of ∼1 arcmin^2 each with a total exposure time of 1 hr per pointing (see the green footprints in Figure 1). Four of the MUSE pointings overlap with the NIRCam fields from the GLASS-JWST ERS program while the fifth targets a prominent cluster substructure at a distance between ∼600 and 775 kpc from the core of A2744 (B23). The extended HST imaging from the BUFFALO program revealed several strong-lensing features around two bright cluster members, subsequently confirmed by the new JWST imaging (F23).

The MUSE data cubes have been reduced and analyzed following Caminha et al. (2017a, 2017b, 2019), using the standard reduction pipeline (version 2.8.5; Weilbacher et al. 2020). The "autocalibration" method and the Zurich Atmosphere Purge (ZAP; Soto et al. 2016) are then applied to improve the overall data reduction. The five pointings have a mean FWHM value of $0\farcs75$, and the pointing covering the cluster substructure has a value of FWHM = $0\farcs86$.

The one-dimensional spectra of all the HST-detected objects are extracted within a $0\farcs8$ radius circular aperture, whereas custom apertures are considered for faint sources, based on their estimated morphology from the HST imaging (see Section 2.1). For sources with no HST detection (i.e., HST-dark objects) we visually inspect the continuum subtracted data cubes to identify emission lines. We exploit spectral templates, as well as the identification of emission lines, to construct the new redshift catalogs. The reliability of each redshift measurement is then quantified with the following quality flag (QF) assignments (see also Balestra et al. 2016; Caminha et al. 2019): "tentative" (QF = 1), "likely" (QF = 2), "secure" (QF = 3), and "based on a single emission line" (QF = 9).

The full spectroscopic sample from the MUSE DDT program contains 313 reliable (i.e., QF ⩾2) redshift measurements, of which 12 are stars, 12 are foreground galaxies ($z < 0.28$), 82 are cluster members ($0.28 \leqslant z \leqslant 0.34$), and 207 are background objects ($z > 0.34$). The redshift distributions of the spectroscopic cluster members and background galaxies from the MUSE DDT observations are shown in Figures 2 and 3, respectively. We note that 42 UV-faint $z \sim 3$–7 galaxies have been published by Prieto-Lyon et al. (2023). The full catalog is presented in Table 3 in Appendix B.

[26] This corresponds to a difference of $\Delta(\text{R.A., decl.})_{\text{HFF}-\text{JWST}} = (0\farcs02, -0\farcs07)$.

[27] https://archive.stsci.edu/prepds/frontier/

[28] https://glass.astro.ucla.edu/ers/external_data.html

[29] archive.stsci.edu/prepds/glass/

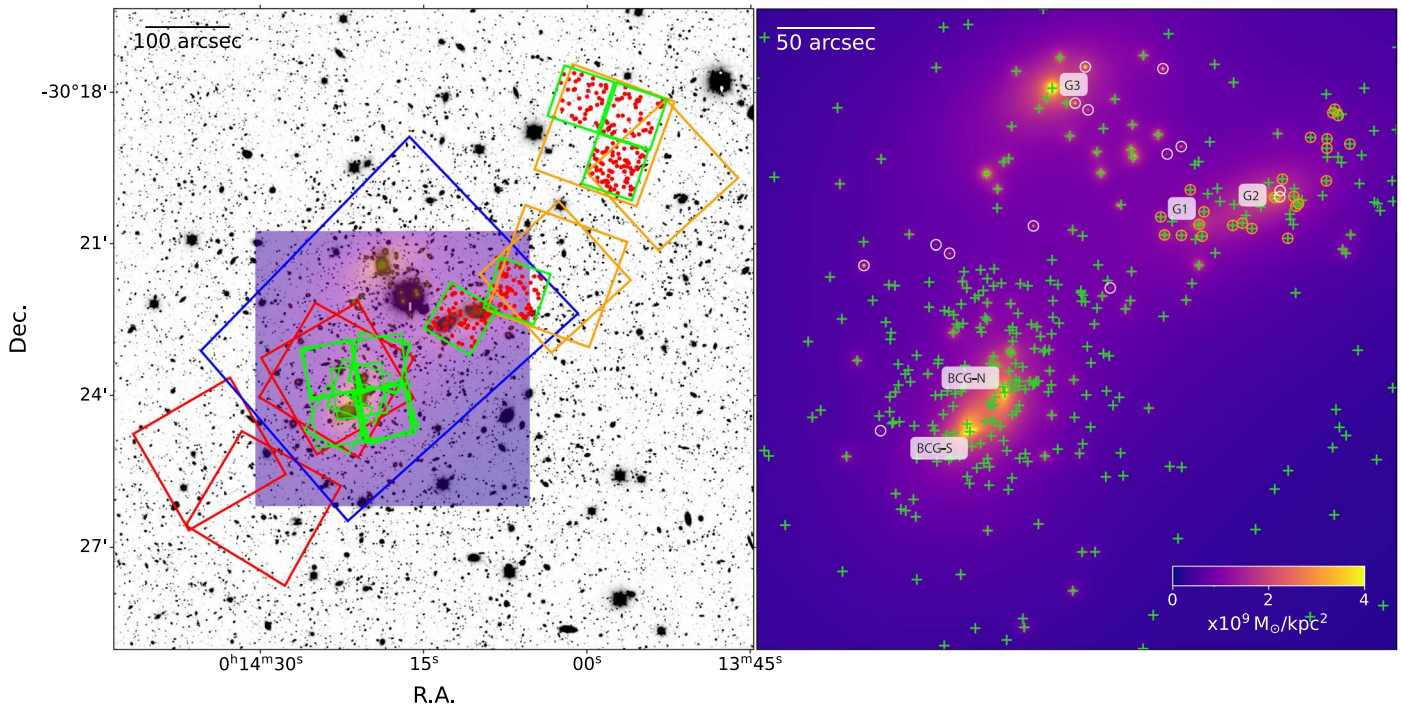

Figure 1. JWST/NIRCam and VLT/MUSE pointings observed for the galaxy cluster A2744 and the projected total mass density distribution obtained from the extended lens model presented in this work. Left: Magellan r-band image of the galaxy cluster A2744. The footprints of the NIRCam pointings observed during the GLASS-JWST ERS, UNCOVER, and DDT 2756 programs are shown in orange, blue, and red, respectively. The footprints of the MUSE pointings are drawn in green. The purple squared region represents the 5.5×5.5 arcmin^2 area covered by the extended lens model. Red dots show the 313 newly determined secure redshifts from the MUSE DDT observations. Right: projected total mass density distribution of A2744 obtained from the extended lens model. The green crosses mark the position of the 669 spectroscopically confirmed cluster member galaxies, corresponding to the light-gray histogram in Figure 2. We note that only the galaxies residing in purple area are shown in the plot. Of the spectroscopic cluster galaxies, 163 with $m_{\rm F160W} < 21$, plus 14 nonspectroscopically confirmed galaxies (white circles), are included in the lens model. The 24 cluster galaxies included in the lens model with a new spectroscopic confirmation from the MUSE DDT data are encircled in orange.

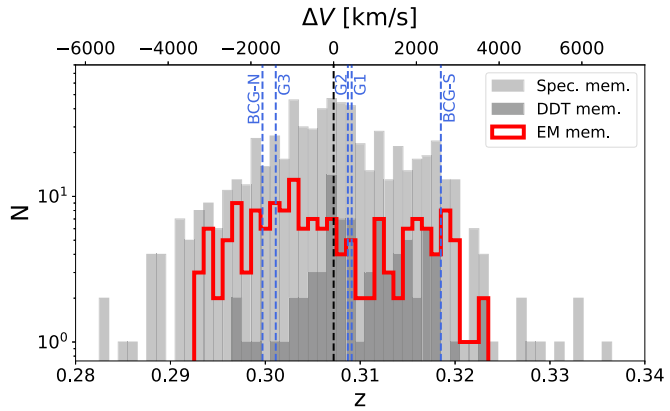

Figure 2. Redshift distribution of the spectroscopic cluster member galaxies of A2744. The redshift distribution of all the spectroscopically confirmed cluster galaxies within the redshift interval $0.28 \leqslant z \leqslant 0.34$ is plotted using the light-gray histogram (669 galaxies). The dark-gray histogram corresponds to the distribution of the newly identified members, with secure redshift values, measured from the DDT MUSE data (82 galaxies). The red histogram shows the redshift distribution of the spectroscopically confirmed cluster member galaxies brighter than $m_{\rm F160W} = 21$ considered in the lens model (163 galaxies; see also Figure 1).

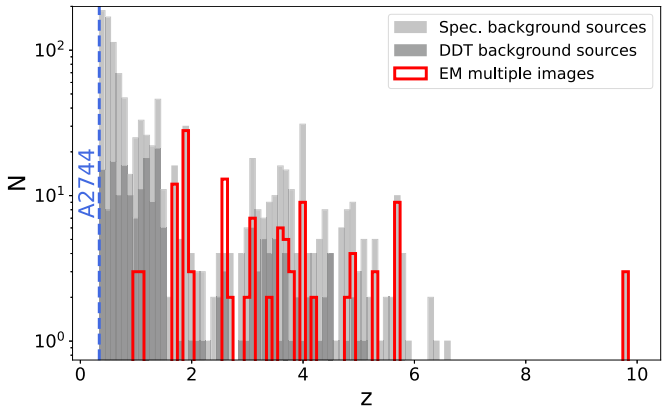

Figure 3. Redshift distribution of all the sources with a secure spectroscopic redshift higher than the A2744 cluster redshift. The redshift distribution of all the galaxies with $z > 0.34$ is plotted as the light-gray histogram. The dark-gray histogram corresponds to the distribution of the background sources with secure redshift values measured from the new DDT MUSE data. The red histogram shows the redshift distribution of the spectroscopically confirmed multiple images considered in the lens model. All of the 121 spectroscopic multiple images, including the lensed galaxy substructures, are included in the plot (see also Figure 5).

3. Extended Strong-lensing Model

In this section we describe the new strong-lensing model of A2744 making use of the new imaging and spectroscopic data sets presented in Section 2. In particular, thanks to the deep JWST imaging and the MUSE DDT follow-up observations, we are able to expand the samples of multiple images and spectroscopic cluster members compared to the model presented by B23. We use the publicly available strong-lensing modeling pipeline `LensTool`[30] (Kneib et al. 1996; Jullo & Kneib 2009), which reconstructs the total mass distribution of a galaxy cluster implementing a Bayesian technique. We note

[30] https://projets.lam.fr/projects/lenstool/wiki

that the lens model adopts the new JWST astrometric grid, tied to Gaia DR3 (see Section 2.1).

3.1. Parameterization of the Cluster Total Mass

Thanks to the identification of a large number of multiple images in the external clumps (see Section 3.2), we are able to improve the characterization of the total mass distribution of A2744 compared to our previous, HST-based strong-lensing model by B23. The total mass parameterization of the cluster core is the same as the one adopted by B23. We thus refer the reader to that publication for a detailed description and provide hereafter a brief summary. Within the parametric `LensTool` software (Jullo et al. 2007), the total mass of the lens is separated into several components, where the following mass contributions are considered in this analysis (we note that our lens model does not include an external shear term):

$$\phi_{\rm tot} = \sum_{i=1}^{N_h} \phi_i^{\rm halo} + \sum_{j=1}^{N_{\rm BCG}} \phi_j^{\rm BCG} + \sum_{k=1}^{N_g} \phi_k^{\rm gal} + \sum_{l=1}^{N_s} \phi_l^{\rm ENV}. \quad (1)$$

The cluster and subhalo mass components ($\phi^{\rm halo}$, $\phi^{\rm BCG}$, and $\phi^{\rm gal}$) are parameterized using dual pseudoisothermal elliptical mass distributions (dPIEs; Limousin et al. 2005; Elíasdóttir et al. 2007; Bergamini et al. 2019). The dPIE profile is defined by seven free parameters: the position (x, y); the ellipticity (defined as $e = \frac{a^2-b^2}{a^2+b^2}$, where a and b are the values of the major and minor semiaxes, respectively); the position angle θ, computed counterclockwise from the west direction; the central velocity dispersion σ_0[31]; the core radius $r_{\rm core}$; and the truncation radius $r_{\rm cut}$.

The large-scale dark matter component, $\phi^{\rm halo}$, consists of two nontruncated elliptical dPIEs, which are initially centered on the two brightest cluster galaxies (BCGs; labeled BCG-N and BCG-S) but are free to move within a small range around their positions (corresponding to square regions of sizes of about 45 kpc and 90 kpc for the BCG-N and BCG-S, respectively; see Table 1). As pointed out by B23, the observed positions of several multiple-image systems with small angular separation from the BCG-N and BCG-S are better reproduced when the parameters describing their mass contribution—$\phi^{\rm BCG}$ and ellipticity—are optimized outside the scaling relations adopted for the other cluster members, as discussed below. BCGs are known to be uncommon galaxies and their independent modeling highlights the importance of the two BCGs for an accurate lensing analysis.

Of the 177 cluster member galaxies (see Section 3.3), 172 are modeled using circular dPIEs with a vanishing core radius and scaled with total mass-to-light ratios increasing with their HST F160W luminosities: $M_T L^{-1} \propto L^{\gamma}$, with $\gamma = 0.2$, i.e., a relation that is compatible with the so-called tilt of the fundamental plane (e.g., Faber et al. 1987; Bender et al. 1992), as done by B23 (see their Equation (4)). The two free parameters in the lens model are then the values of the velocity dispersion and truncation radius of a reference galaxy, corresponding to the BCG-N. We report in Table 1 the values of the relevant parameters of the scaling relations. B23 further exploited the MUSE data cube to measure the line-of-sight stellar velocity dispersion for 85 member galaxies, down to $m_{\rm F160W} \sim 22$, allowing for an independent calibration of the slopes of the velocity dispersion, α, and truncation radius scaling relations, $\beta_{\rm cut}$ (see B23 for details).

As previously mentioned, the main difference with respect to the strong-lensing analysis presented by B23 is the modeling of the cluster infalling regions, $\phi^{\rm ENV}$. Due to the lack of secure multiple-image systems around the massive structures in the northwestern region of the cluster prior to the JWST/NIRCam imaging, the B23 reference `LM-model` included a simple description of the mass contribution from three external clumps, associated with the three brightest galaxies (G1, G2, and G3), as singular isothermal sphere (SIS) profiles. The identification of 29 (3) multiple images around galaxies G1–G2 (G3) allows now for a more accurate total mass reconstruction of these infalling structures, $\phi^{\rm ENV}$, which is decomposed into the following mass contributions:

$$\phi^{\rm ENV} = \phi^{\rm halo}_{\rm G1-G2} + \phi^{\rm halo}_{\rm G3} + \phi_{\rm G1} + \phi_{\rm G2} + \phi_{\rm G3}. \quad (2)$$

The first two terms correspond to the cluster component that is modeled as two cluster-scale nontruncated elliptical dPIEs: one associated with galaxies G1 and G2 and allowed to move within a large square region containing the two galaxies (see Table 1; corresponding to a region of about 270 kpc × 180 kpc), and a second one centered on the position of galaxy G3. The parameters describing the mass contribution (i.e., the velocity dispersion and cut radius) of the three galaxies G1, G2, and G3 are individually optimized, within large flat priors. In addition, the ellipticity parameters of G1 and G2 are left free to vary (see Table 1). As mentioned in Section 3.3, the parametric description of the cluster outskirts is further enhanced by the inclusion of a sample of spectroscopic cluster members from the new MUSE/DDT observations (see Figure 1 and Section 3.3).

Finally, the redshifts of the eight photometric multiple-image systems are also optimized in the lens model within uninformative flat priors. We note that the redshift value of all the images of Sys-200 (i.e., A200.1a,b, B200.2a,b, and C200.3a,b) is imposed to be equal in the optimization of the lens model (and therefore corresponding to a single free parameter).

The priors assumed for the values of the parameters of the mass profiles included in our reference lens model are reported in the upper part of Table 1, while the optimized values are provided in the bottom panel. The best-fitting values of the model parameters that describe the total mass distribution of the lens are obtained by minimizing on the image plane the distance between the observed and the model-predicted point-like positions of the multiple images through a χ^2 function (see Equation (1) in B23). Following B23, we assign an initial positional uncertainty to each image depending on the value of the positional quality flag (QP), which are given in Table 2. These values are then rescaled, prior to the sampling of the posterior distributions, in order to obtain a χ^2 value close to the number of degrees of freedom (dof) in the model, defined as: $\mathrm{dof} = 2 \times [N_{\rm im}^{\rm tot} - N_{\rm fam}] - N_{\rm freepar} = N_{\rm con} - N_{\rm freepar}$, where $N_{\rm im}^{\rm tot}$ and $N_{\rm fam}$ refer, respectively, to the total number of multiple images and families included in the lens model. The term $2 \times N_{\rm fam}$ represents the model parameters associated with the sources positions. $N_{\rm con}$ and $N_{\rm freepar}$ are the number of model constraints and free parameters, respectively. The total mass model of A2744 has $N_{\rm freepar} = 50$ free parameters, including the eight optimized redshifts of the nonspectroscopic systems, leading to 148 dof. This model represents an extension of that

[31] `LensTool` adopts a scaled version of this quantity, identified as $\sigma_{\rm LT}$, such that $\sigma_{\rm LT} = \sigma_0 \sqrt{2/3}$.

Table 1
Input and Output Parameters of the Extended Lens Model for the Galaxy Cluster A2744 Presented in This Work

		Input Parameter Values and Assumed Priors						
		x (arcsec)	y (arcsec)	e	θ (°)	$\sigma_{\rm LT}$ (km s^{-1})	$r_{\rm core}$ (arcsec)	$r_{\rm cut}$ (arcsec)
Cluster-scale Halos	1st Cluster Halo	$-5.0 \div 5.0$	$-5.0 \div 5.0$	$0.0 \div 0.9$	$0.0 \div 180.0$	$300 \div 1500$	$0.0 \div 30.0$	2000.0
	2nd Cluster Halo	$-27.9 \div -7.9$	$-30.0 \div -10.0$	$0.0 \div 0.9$	$0.0 \div 90.0$	$300 \div 1500$	$0.0 \div 30.0$	2000.0
	G1,G2 Halo	$90.0 \div 150.0$	$80.0 \div 120.0$	$0.0 \div 0.9$	$0.0 \div 180.0$	$300 \div 1500$	$0.0 \div 30.0$	2000.0
	G3 Halo	24.2	155.8	$0.0 \div 0.9$	$0.0 \div 180.0$	$100 \div 1500$	$0.0 \div 30.0$	2000.0
Subhalos	BCG-N	0.0	0.0	$0.0 \div 0.9$	$0.0 \div 180.0$	$200 \div 400$	0.0001	$0.1 \div 50.0$
	BCG-S	−17.9	−20.0	$0.0 \div 0.9$	$0.0 \div 180.0$	$200 \div 400$	0.0001	$0.1 \div 50.0$
	G1	99.4	85.9	$0.0 \div 0.9$	$0.0 \div 180.0$	$150 \div 350$	0.0001	$0.1 \div 50.0$
	G2	138.3	99.8	$0.0 \div 0.9$	$0.0 \div 180.0$	$150 \div 350$	0.0001	$0.1 \div 50.0$
	G3	24.2	155.8	0.0	0.0	$150 \div 400$	0.0001	$0.1 \div 50.0$
	Scaling Relations	$N_{\rm gal} = 172$	$m^{\rm ref}_{\rm F160W} = 17.34$	$\alpha = 0.40$	$\sigma^{\rm ref}_{\rm LT} = 190 \div 300$	$\beta_{\rm cut} = 0.41$	$r^{\rm ref}_{\rm cut} = 0.5 \div 10.0$	$\gamma = 0.20$

		Optimized Output Parameters						
		x (arcsec)	y (arcsec)	e	θ [°]	$\sigma_{\rm LT}$ [km s^{-1}]	$r_{\rm core}$ (arcsec)	$r_{\rm cut}$ (arcsec)
Cluster-scale Halos	1st Cluster Halo	$-1.8^{+0.6}_{-0.6}$	$-3.5^{+1.4}_{-1.1}$	$0.4^{+0.1}_{-0.1}$	$79.0^{+5.3}_{-7.0}$	558^{+33}_{-35}	$9.3^{+1.1}_{-1.1}$	2000.0
	2nd Cluster Halo	$-18.7^{+0.5}_{-0.4}$	$-16.3^{+0.5}_{-0.5}$	$0.4^{+0.1}_{-0.1}$	$55.2^{+2.8}_{-2.7}$	603^{+25}_{-25}	$8.1^{+0.6}_{-0.6}$	2000.0
	G1,G2 Halo	$130.2^{+2.2}_{-2.8}$	$97.9^{+0.8}_{-1.1}$	$0.7^{+0.1}_{-0.1}$	$23.8^{+2.1}_{-1.9}$	781^{+35}_{-38}	$16.8^{+2.0}_{-2.0}$	2000.0
	G3 Halo	24.2	155.8	$0.1^{+0.2}_{-0.1}$	$14.1^{+25.7}_{-67.1}$	799^{+40}_{-37}	$22.9^{+3.8}_{-4.4}$	2000.0
Subhalos	BCG-N	0.0	0.0	$0.6^{+0.1}_{-0.2}$	$87.5^{+5.8}_{-8.1}$	266^{+15}_{-12}	0.0001	$31.8^{+11.6}_{-12.1}$
	BCG-S	−17.9	−20.0	$0.7^{+0.1}_{-0.1}$	$23.7^{+3.3}_{-3.3}$	296^{+12}_{-14}	0.0001	$44.9^{+3.7}_{-7.1}$
	G1	99.4	85.9	$0.3^{+0.3}_{-0.2}$	$17.3^{+21.5}_{-54.6}$	232^{+16}_{-18}	0.0001	$29.0^{+11.0}_{-9.7}$
	G2	138.3	99.8	$0.4^{+0.2}_{-0.2}$	$-14.0^{+14.7}_{-19.8}$	231^{+15}_{-16}	0.0001	$23.3^{+13.2}_{-11.5}$
	G3	24.2	155.8	0.0	0.0	332^{+38}_{-38}	0.0001	$13.4^{+8.4}_{-6.3}$
	Scaling Relations	$N_{\rm gal} = 172$	$m^{\rm ref}_{\rm F160W} = 17.34$	$\alpha = 0.40$	$\sigma^{\rm ref}_{\rm LT} = 246^{+9}_{-10}$	$\beta_{\rm cut} = 0.41$	$r^{\rm ref}_{\rm cut} = 9.3^{+0.5}_{-1.0}$	$\gamma = 0.20$

Notes. The x and y coordinates are expressed in arcseconds with respect to the position of the BCG-N, at R.A. = 3.586244, decl. = −30.400151. In the input parameter table, single numbers are quoted for parameters that are kept fixed during the model optimization. When two values (separated by the ÷ symbol) are quoted for a parameter, they correspond to the boundaries of the flat prior assumed in the model. $N_{\rm gal}$ is the number of cluster member galaxies optimized through the scaling relations (see Equation (4) in B23). In the last line of each table, we report the reference magnitude, $m^{\rm ref}_{\rm F160W}$, and the remaining parameters of the scaling relations. In particular, α and $\beta_{\rm cut}$ represent the slopes of the velocity dispersion and truncation radius scaling relations, respectively, while γ relates the total mass-to-light ratio to the luminosity of the galaxies. In the output parameter table, we quote the optimized values of the model parameters. For each free parameter, we quote the median and the 16th, and 84th percentiles from the model marginalized posterior distributions. The posterior distributions of the angular parameter θ of the G3 halo and of galaxies G1 and G2 are remapped to an angular interval between −90° and 90° before computing the percentiles.

presented by B23 and thus is labeled as such in the following (`Extended Model` or EM).

3.2. Multiple-image Catalog

This work extends the multiple-image catalog presented by B23, which was based on the deep HST imaging and MUSE observations of the cluster core. The B23 sample consisted of 90 multiple images from 30 background sources, spanning a redshift range between $z = 1.69$ and $z = 5.73$. For further details, we refer the reader to Table A.1 of B23. By exploiting the ancillary and the recently obtained JWST/NIRCam imaging and new VLT/MUSE data, we identify additional multiple images both in the cluster core and in the external clumps.

Our new strong-lensing model includes 149 multiple images from 50 background sources, of which 121 are spectroscopically confirmed and span an extended redshift range between $z = 1.03$ and $z = 9.76$ (see Figure 3). This represents an increase of ∼66% compared to the B23 sample. The cumulative distribution of the distances of both the spectroscopic and photometric multiple images included in the lens model from the BCG-N is shown in Figure 4 (red solid line) in comparison to the one used by F23 (black solid line). The complete sample presented in this work includes 14 more multiple images than that from F23 and thus represents the largest set of constraints included in a lens model of A2744 to date. The set of spectroscopic images is especially noteworthy. In more general terms, A2744 is the second cluster with the largest sample of secure multiple images after the lens cluster MACS J0416.1−2403, which currently counts 237 (Bergamini et al. 2023b). For consistency, we present in Table 2 the properties (in the JWST-based astrometry) of the complete sample of multiple images used as constraints in this work, included those presented by B23. The multiple-image positions are shown in Figure 5, where the crosses (circles) denote the spectroscopic (photometric) images. We briefly describe below the identification of the new multiple images with respect to those from B23.

Cluster core. Following B23, we reanalyze the MUSE data cube, extracting the spectra of sources predicted by the lens

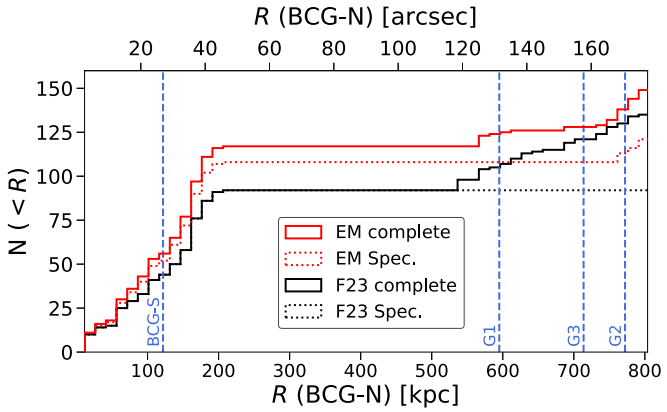

Figure 4. Cumulative distributions of the distances of the multiple images of A2744 from the BCG-N. We show in solid red the distribution of the images used as constraints in this work (149 multiple images in total) and in dotted red the distribution of the 121 spectroscopic images. The distributions of the spectroscopic (90 multiple images, coinciding with those used by B23 in addition to the two images JD1A and JD1B in Table 2) and of the complete (135 multiple images) samples of multiple images used in F23 are shown in black. The distances of the other bright galaxies in the field (i.e., BCG-S, G1, G2, and G3) are indicated with vertical dashed blue lines.

model and measuring the redshift of several multiple images using faint emission lines and the cross correlation with different templates. We thus include 14 additional spectroscopically confirmed multiple images in the cluster core, from five systems. These new images are flagged by a star symbol in Table 2.

Recent JWST observations have allowed for the spectroscopic confirmation of two additional multiple images in the cluster core as part of the GLASS-JWST ERS program (identified by an asterisk in Table 2). While image 3c is too faint for a secure redshift measurement with VLT/MUSE, JWST/NIRISS spectroscopy enables the detection of [O II] λ3727,3729 at the expected wavelength position of 1.856 μm, and consistent with counterimages 3a and 3b (Vanzella et al. 2022; Lin et al. 2023). The $z_{\rm phot} = 9.8$ triply lensed candidate system reported by Zitrin et al. (2014) was observed with NIRSpec prism spectroscopy (DDT 2756; PI: Chen) resulting in a spectroscopic redshift measurement of $9.756^{+0.017}_{-0.007}$ of the image JD1B (Roberts-Borsani et al. 2023). The other two images, JD1A and JD1C, which are not yet spectroscopically confirmed, are considered at the same redshift as JD1B, consistent with their photometric redshifts.

The list of multiple images is further enhanced in the cluster core by including three photometric strongly lensed sources, with a total of nine multiple images, securely identified in the JWST/NIRISS and JWST/NIRCam imaging from the GLASS-JWST ERS program. In particular, Sys-53 consists of a triply imaged active galactic nucleus (AGN) candidate analyzed in Furtak et al. (2022). The very peculiar color and compactness of the source make the association of the three multiple images of the system particularly secure.

The final sample in the main cluster core includes 117 multiple images from 39 background sources, of which 108 are spectroscopically confirmed.

External clumps. The main improvement with respect to B23 is the identification of a large number of multiple images around galaxies G1 and G2 in the northwestern external clump. While the ancillary shallow HST imaging of the cluster outskirts hinted at the presence of strong-lensing features, the recent deep, high-resolution JWST/NIRCam data clinched the identification of several photometric systems. We identify 29 multiple images from 10 background sources around galaxies G1 and G2, and three multiple images from a single background source around galaxy G3. We also include multiply lensed clumps within resolved extended sources, which have shown to be particularly efficient at constraining the position of the critical curves (e.g., Grillo et al. 2016; B23). In particular, thanks to the MUSE DDT observations we are able to measure the redshift of the lensed face-on spiral galaxy (ID 600) around G2. Due to the light contamination by a star and by G2 of the images 600a and 600b, respectively, a secure spectroscopic confirmation is not currently possible for those images. The MUSE spectrum of image 600c, extracted within a circular aperture of 0.″8 diameter, is shown in Figure 6, yielding a redshift measurement of 2.584. This secure redshift is based on the cross correlation of the MUSE spectrum with several spectral templates of star-forming galaxies with appropriate rest-frame UV coverage, which consistently shows a significant peak at the quoted redshift with a variation of $\Delta z = 0.003$. This is, to date, the only multiple-image system spectroscopically confirmed in the northwestern external clump.

The observed image positions of the 149 multiple images are used as constraints in the new lens model, providing in total $N_{\rm con} = 198$ constraints.

3.3. Selection of Cluster Galaxies

For the selection of the cluster galaxies used in the lens model to describe the subhalo mass component, we follow the procedure of B23 taking advantage of the enhanced spectroscopic coverage in the northwestern clump. Initially, cluster members are selected as the galaxies with a spectroscopic redshift in the range $0.28 \leqslant z \leqslant 0.34$, corresponding approximately to an interval of ± 6000 km s^{-1} rest-frame velocities around the median cluster redshift $z_{\rm CL} = 0.3072$, and magnitudes brighter than $m_{\rm F160W} = 24$ (a dedicated work on the properties of cluster members is presented by Vulcani et al. 2023). The larger range in redshift is motivated by the complexity of the total mass distribution of A2744, a multicomponent merger (see, e.g., Merten et al. 2011; Owers et al. 2011). This is clearly shown in Figure 2, where the velocity difference between the BCG-N and BCG-S is of about 4000 km s^{-1}. The new MUSE DDT data add 82 members to the full spectroscopic sample (see Section 2.2), which now includes 669 cluster galaxies, mostly based on the MUSE observations (Richard et al. 2021; B23). When compiling this catalog, we only consider secure or probable/likely redshift measurements from different sources (see Section 2.2). The redshift distribution of the cluster members over the cluster area is shown in Figure 2, while their spatial distribution is shown in the right panel of Figure 1. The spectroscopic sample is then completed down to $m_{\rm F160W} = 24$ by adding the photometric members identified with the convolution neural network (CNN) technique described by Angora et al. (2020). Performance tests generally show a cluster member identification rate (completeness) of ∼90% with a purity of ∼95%, superior to those from traditional color selection methods (Angora et al. 2020).

The large number of cluster galaxies makes the extended lens model presented here computationally very expensive, owing to the calculation of the deflection angle induced by each

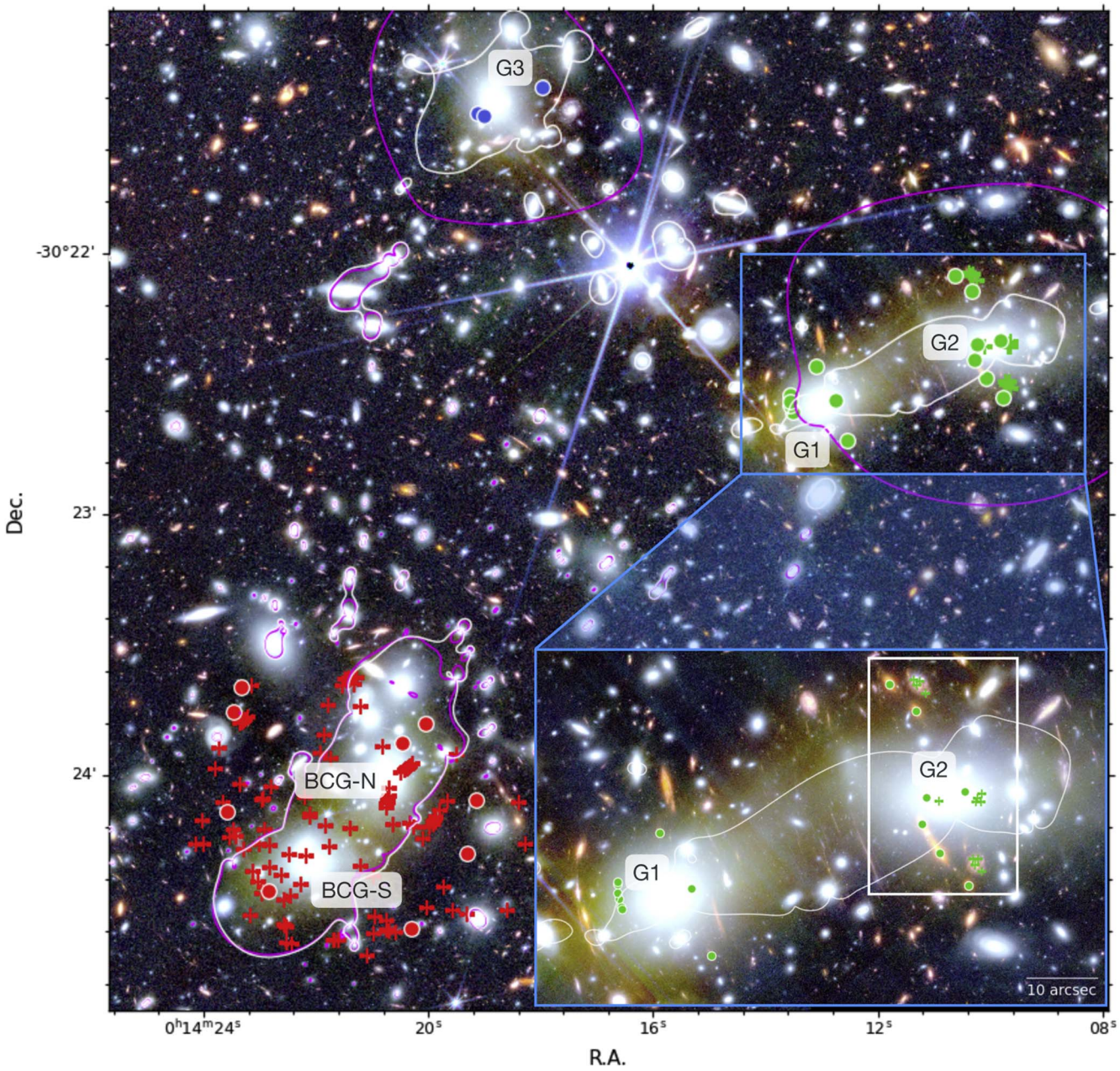

Figure 5. JWST color image (R: F444W+F356W, G: F277W+F200W, B: F150W+F115W) of the galaxy cluster A2744 showing the positions of the 149 multiple images, from 50 background sources, used to constrain the lens model. The colored crosses show the positions of the 121 spectroscopically confirmed multiple images, while the colored circles are the 28 nonspectroscopic multiple images used in the lens model. Red, green, and blue colors highlight the images concentrated around the cluster BCGs (117 multiple images from 39 background sources), the two bright galaxies G1 and G2 (29 multiple images from 10 background sources), and galaxy G3 (three multiple images from a single background source), respectively. The critical lines at $z_s = 6$ obtained from the best-fit lens model are drawn in white, while those from the previous model by B23 are shown in magenta as a comparison.

individual cluster member. With the aim of limiting the computational time increase, we reduce the number of faint cluster galaxies in the lens model and study how the positional rms value, $\Delta_{\rm rms}$, varies when considering different magnitude threshold values for the cluster members in the F160W band. We find no significant variation in $\Delta_{\rm rms}$ when only including in the model the galaxies with magnitudes $m_{\rm F160W} < 21$ and thus, we limit the number of cluster galaxies to those brighter than $m_{\rm F160W} = 21$. A similar finding is presented by Raney et al. (2021), which shows that considering different magnitude limits for the selection of member galaxies in the lens models of two HFF clusters, between 21 and 26 in the F814W band, results in little variations in the values of $\Delta_{\rm rms}$ or other metrics (see their Figure 4).

With the new magnitude cut, $m_{\rm F160W} = 21$, 163 spectroscopic members are included in the lens model (see the red histogram in Figure 2), in addition to 14 nonspectroscopic galaxies, over an area of $\sim$30 arcmin^2. The new spectroscopic cluster members are concentrated in the NW mass clumps, around G1, G2, and G3 (see Figure 1). As a comparison, the B23 strong-lensing model included 225 members with a limit three magnitudes fainter.

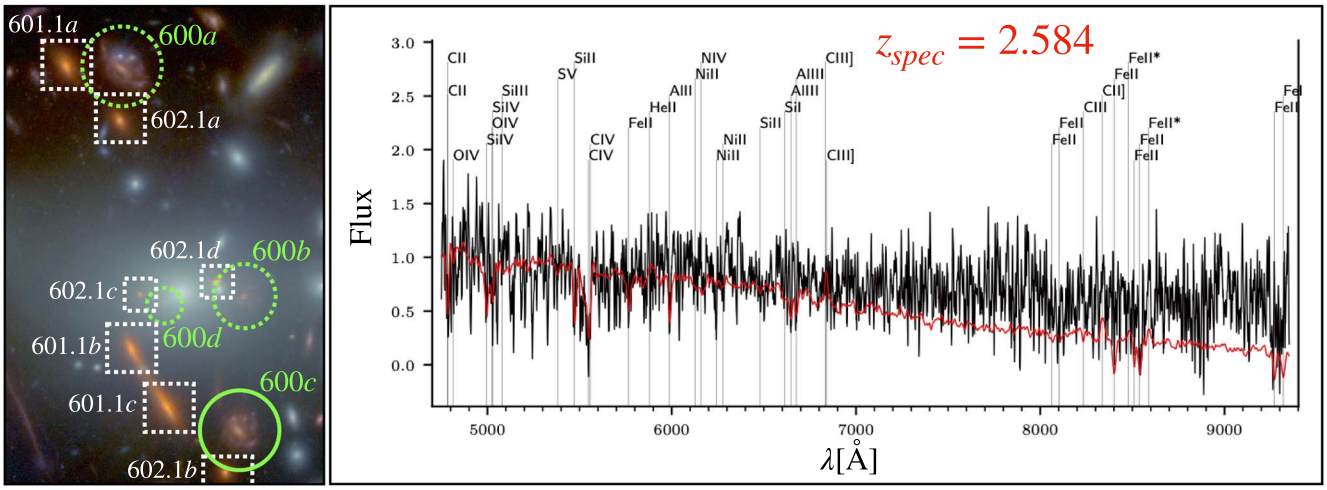

Figure 6. MUSE spectrum of the multiple image 600c (containing the multiply imaged substructures 600.1c, 600.3c, 600.4c, and 600.5c) overlaid to a star-forming template from Talia et al. (2012; red line). This system is a face-on spiral at $z = 2.584$ marked as a solid green circle in the left panel (corresponding to the white box in Figure 5 around G2). Three other images of the system (600a,b,d) are indicated as dashed green circles; white dotted squares show the multiple images 601.1a,b,c and 602.1a,b,c,d with no spectroscopic redshifts (see Figure 10 and Table 2).

4. Results

The best-fit `Extended Model` is characterized by a precision of $\Delta_{\rm rms}^{\rm TOT} = 0\farcs43$ in reproducing the observed positions of the 149 multiple images used as constraints in the lens model (see Section 3.1). This is a remarkable result given the significantly larger number of multiple images compared to previous lens models (e.g., 59 more than in B23), the complexity of the cluster total mass distribution, and the large modeled area. In Figure 7, we show for each multiple image the displacement Δ_i between its observed and model-predicted positions. To quantify the precision of the lens model around the three main massive structures within the considered area (see Figure 1), we adopt different colors to distinguish the multiple images forming around the main cluster BCGs (red), the two bright galaxies G1 and G2 (green), and cluster galaxy G3 (blue). We note that the same color scheme is adopted in Figure 5 to indicate the observed positions of the multiple images. The positions of the 117 multiple images forming around the main cluster BCGs are reproduced with a precision of $\Delta_{\rm rms}^{\rm BCGs} = 0\farcs46$. This value is just $0\farcs09$ larger than that obtained using the previous model by B23, which included 27 fewer multiple images in the same region. An even higher precision of $\Delta_{\rm rms}^{\rm G1,G2} = 0\farcs20$ is found in reproducing the observed positions of the 29 multiple images forming around G1 and G2. In contrast, the EM precision decreases to $\Delta_{\rm rms}^{\rm G3} = 0\farcs73$ around galaxy G3. Here, only three nonspectroscopic images (700.a, 700.b, and 700.c) of a single background galaxy are included in the lens model. We notice that the deflecting contribution of the massive clump surrounding G3 is mainly driven by its influence on the many multiple images observed relatively far from its center, i.e., in the cluster core. For this reason, the optimized values of the parameters of this clump might not be able to reproduce as well as for the other sources the three multiple images appearing close to its center.

A further confirmation of our previous results comes from the cumulative projected total mass profiles, presented in Figure 8. These profiles and the associated statistical errors are computed considering 500 realizations obtained by randomly extracting parameter samples from the EM MCMC chains. The black and red solid lines correspond to the median mass

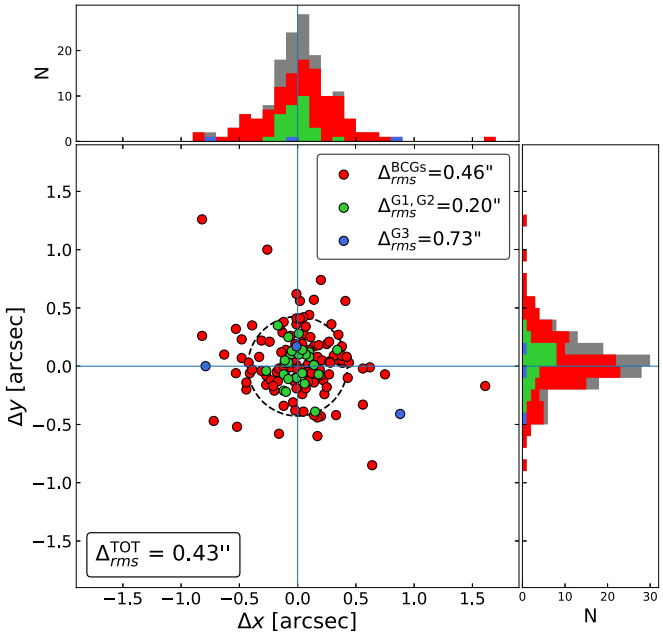

Figure 7. Displacements, Δ_i, along the x and y directions between the observed and model-predicted positions of the 149 multiple images (from 50 background sources) included in the lens model. The lens model is characterized by $\Delta_{\rm rms}^{\rm TOT} = 0\farcs43$, which corresponds to the radius of the black dashed circle. The 117 multiple images, from 39 background sources, concentrated around the two BCGs are plotted in red and have a $\Delta_{\rm rms} = 0\farcs46$. Similarly, the 29 multiple images (from 10 background sources) forming around the two bright galaxies G1 and G2 (with $\Delta_{\rm rms} = 0\farcs20$), and the three multiple images (from a single background source) around galaxy G3 (with $\Delta_{\rm rms} = 0\farcs73$) are plotted in green and blue, respectively. The gray histograms refer to the complete sample of multiple images.

profiles, while the colored shaded bands are limited by the 16th and 84th percentiles. Thanks to the large number of spectroscopically confirmed multiple images observed around the main cluster core, the total mass distribution of the cluster is reconstructed robustly in this region (top-left panel of the figure). This results in a cumulative projected total mass profile measured with very small statistical errors (black band in the figure). By comparing the results from this EM with those

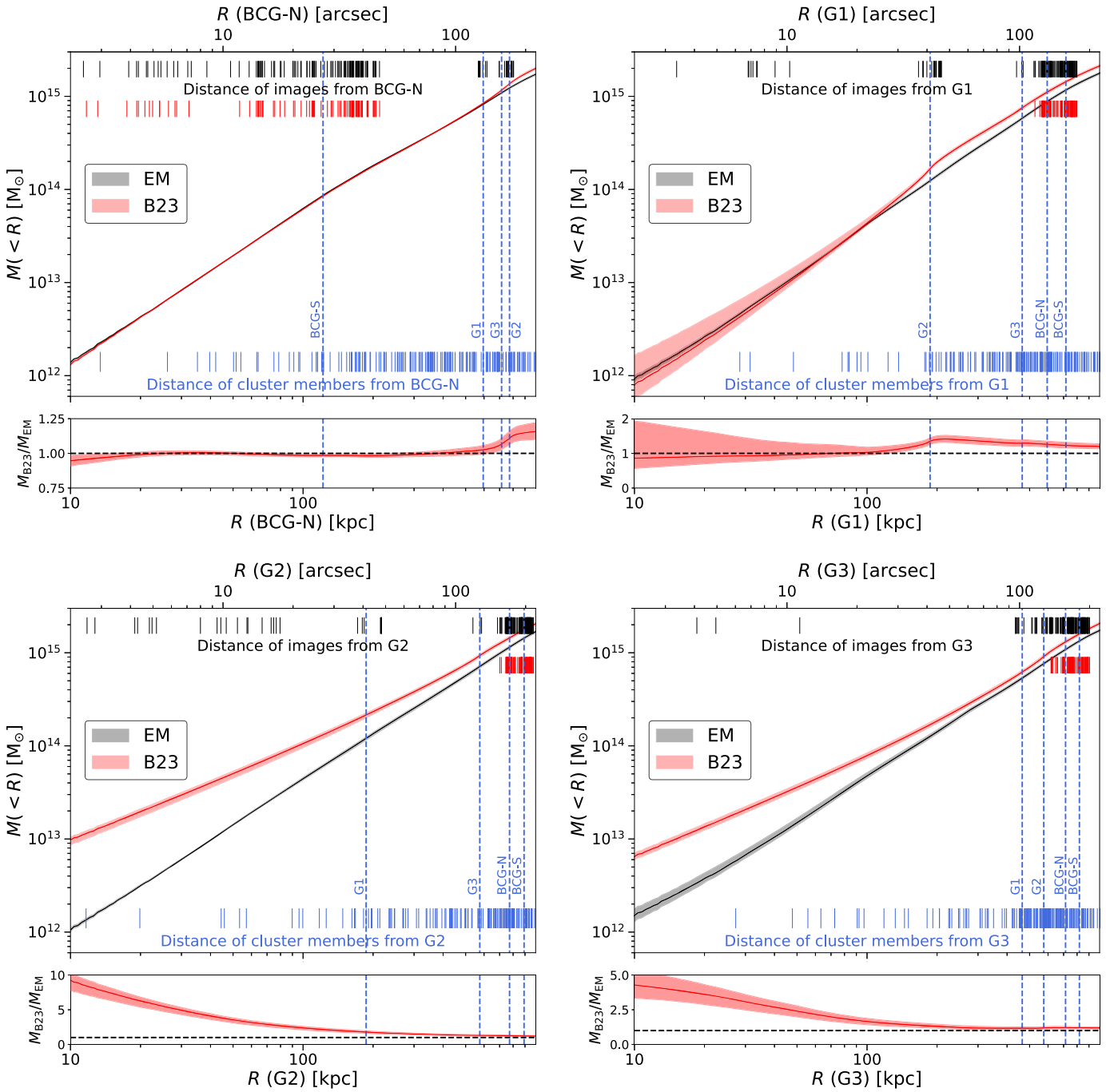

Figure 8. Cumulative projected total mass profiles of galaxy cluster A2744 as a function of the projected distance from the bright galaxies BCG-N (top left), G1 (top right), G2 (bottom left), and G3 (bottom right). The mass profiles obtained from the extended lens model (EM) are drawn in black. The small vertical black and blue bars show the projected distances of the observed multiple images and of the cluster member galaxies considered in the model, respectively. We also highlight, using vertical dashed lines, the positions of the bright cluster galaxies BCG-N, BCG-S, G1, G2, and G3. In red, we plot the cumulative projected total mass profiles from the previous lens model by B23. The projected distances of the multiple images constraining that model are marked with small vertical red bars. At the bottom of each panel, we show the ratio between the total mass profiles obtained from the B23 model and the extended model presented here.

by B23, we find a remarkably good agreement. In particular, the cumulative projected total mass profiles of the two models differ by less than 3% close to the BCG-N core and less than 1% at distances between 20 kpc and 310 kpc. Unsurprisingly, larger differences are found in the regions surrounding the three external clumps. On the top-right and bottom-left panels of Figure 8, we plot the cumulative projected total mass profiles as a function of the distance from the G1 and G2 galaxies, respectively. These profiles demonstrate that the inclusion in the EM of the multiple images identified with JWST/NIRCam imaging around G1 and G2 reduces significantly the statistical uncertainty in the total mass estimates. This is evidenced by the smaller extension of the black bands with respect to the red ones. While the total mass profile around G1 is compatible with the previous result by B23, a clear difference between the total mass profiles is found in the vicinity of G2. The newly

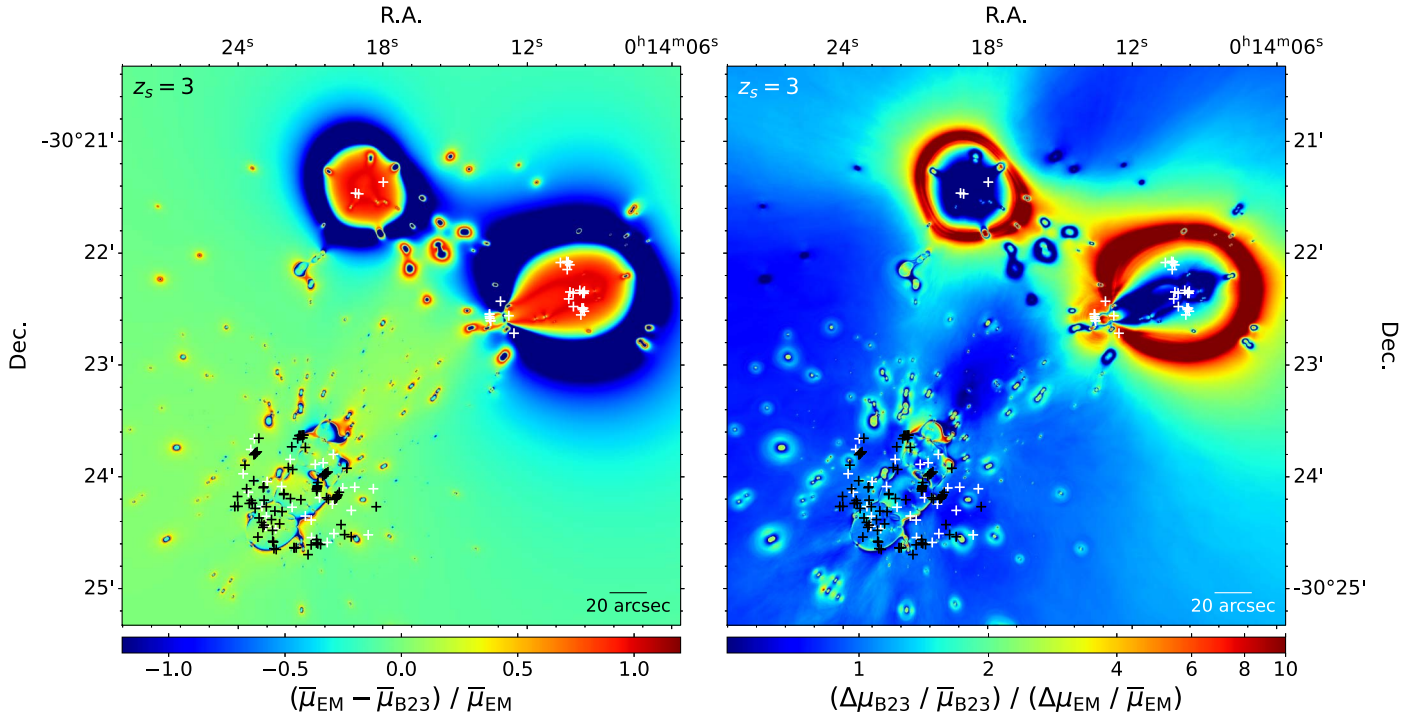

Figure 9. Comparison between the magnification factors, and related errors, obtained from the A2744 extended lens model presented in this paper and the previous model by B23. The black crosses indicate the observed positions of the 90 multiple images used in B23. The white crosses indicate instead those for the 59 new multiple images from this work. Left: relative difference between the median magnification maps (see Section 4) obtained from the extended and B23 lens models. Right: ratio between the relative errors on the magnification maps values estimated from 500 realizations of the lens models obtained by randomly extracting parameter samples from the model MCMC chains.

identified multiple images around G1 and G2—especially the 13 lensed substructures of the spectroscopically confirmed spiral galaxy at $z = 2.584$ (see Figure 6)—are thus key to precisely reconstructing the total mass distribution in this region. Similarly, we remark a large discrepancy between the total mass profiles obtained from the EM and the B23 model, as displayed in the bottom-right panel of Figure 8. In this case, the three nonspectroscopic multiple images, from a single background source, lying close to galaxy G3 can only poorly constrain the total mass distribution of the G3 halo. This is reflected into the black error band, which is more extended than those in the other panels. We remark that the new subhalo scaling relation is consistent over more than five magnitudes with that measured by B23 with MUSE spectroscopy, within the 1σ statistical uncertainties (see Table 1 and their Figure 4). This highlights the importance of an independent determination of the scaling relation in reducing inherent model degeneracies between the cluster and subhalo mass components.

On the left panel of Figure 9, we show the relative difference between the median magnification values derived from the EM ($\overline{\mu}_{EX}$) and B23 model ($\overline{\mu}_{B23}$). The median magnification maps are obtained by considering 500 random realizations of the lens models and computing the median magnification value in each pixel. The right panel of Figure 9 shows instead the ratio of the relative errors on the predicted magnification values for the two models. In this case, the absolute errors $\Delta\mu_{EM}$ and $\Delta\mu_{B22}$ are computed from the 16th and 84th percentiles of the magnification distributions in each pixel.

In the region surrounding the main cluster, the EM and B23 models predict very similar magnification values and associated errors (see the bottom-left region in the maps). This result is corroborated by the similarity of the B23 (magenta) and EM (white) critical lines displayed in Figure 5 for a source at $z_s = 6$. Within the main cluster, nonnegligible differences between the predicted magnification are observed only at distances beyond $\sim 28''$ northwest from the BCG-N, a region deprived of observed multiple images. The main cluster critical line predicted by the best-fit EM becomes resonant with the secondary critical lines produced by two bright galaxies. The consistency between the B23 and EM models in the main cluster region demonstrates that the modeling parameterization from B23 is well suited to robustly characterize its total mass distribution. As expected, closer to the external clumps surrounding galaxies G1, G2, and G3 (in the top and top-right regions of Figure 9) the differences between the EM and B23 models are significant. In particular, the magnification maps reach relative differences of more than $\pm 100\%$ in addition to the significant discrepancy on the shape of the critical lines. In fact, the critical lines obtained by the new EM are significantly more centrally concentrated with respect to the large critical lines produced by the simplistic SIS mass distributions used by B23 to parameterize the external clumps, illustrating the importance of adding strong-lensing constraints in those regions. The right panel of Figure 9 demonstrates that the EM model is characterized by similar relative errors to B23 in the main cluster region in predicting the magnification values, whereas significantly smaller relative errors are found around the external clumps compared to B23. Particular attention has to be paid to the red ring-like and dark blue areas centered on the external clumps. These regions wrap the critical lines of the B23 model and EM computed for a source at $z_s = 3$ (corresponding to the redshift of the magnification

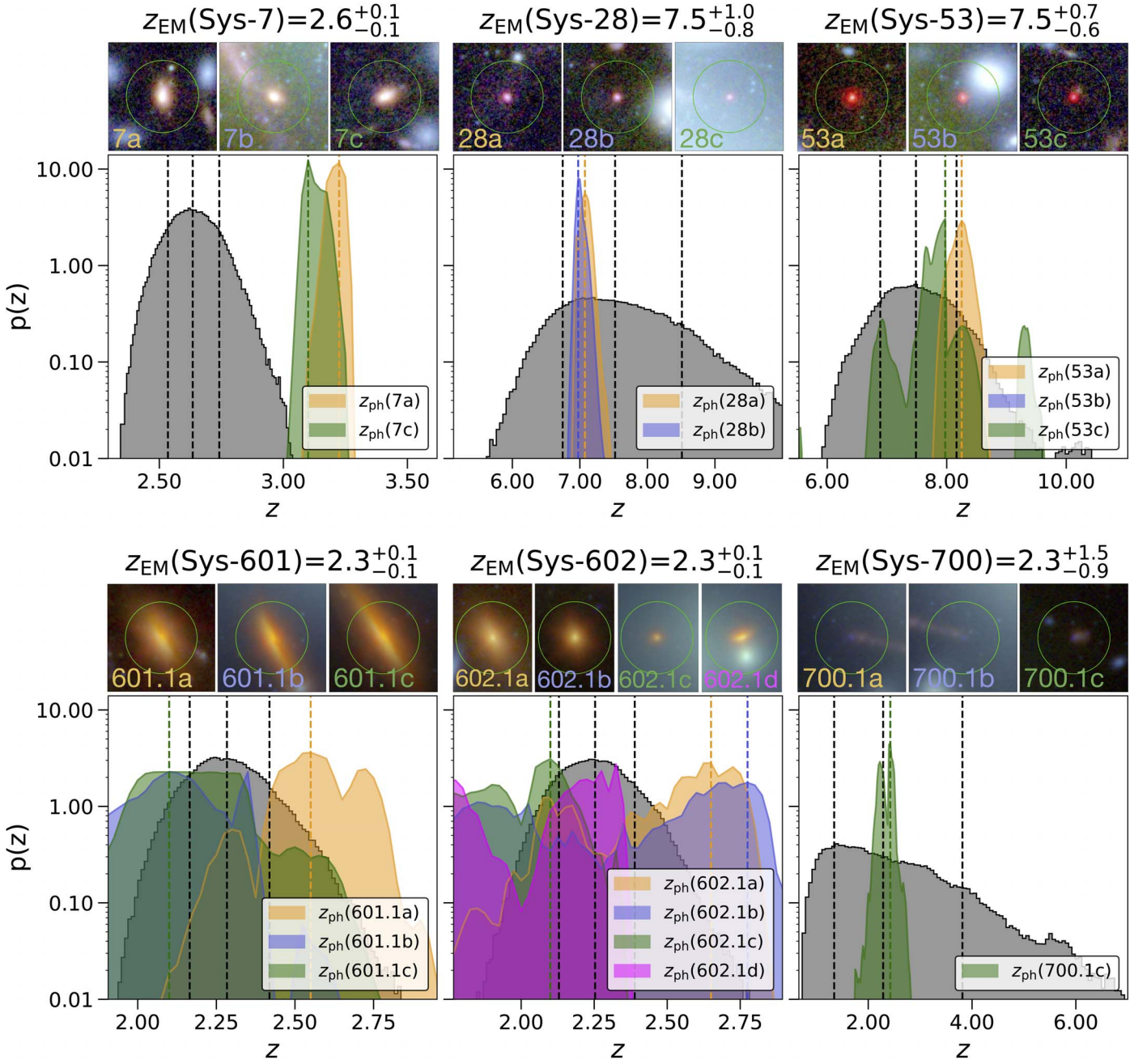

Figure 10. Probability density distributions for the redshift values of the six nonspectroscopic systems of multiple images included in the lens model. The gray histograms correspond to the marginalized probability distributions obtained from the lens model optimization. The orange, blue, green, and magenta distributions represent the photometric redshift probability density distributions measured for the multiple images of the same system. On the top of the histograms, we show color cutouts centered on the corresponding multiple images; the green circles have a radius of 1″. The remaining two nonspectroscopic systems of multiple images considered in the lens model have optimized redshift values of $z_{EM}(\mathrm{Sys}-200) = 5.9^{+2.4}_{-2.3}$ and $z_{EM}(\mathrm{Sys}-301) = 4.1^{+1.2}_{-1.2}$. None of their images have a measured photometric redshift.

maps). We note that the magnification values presented by Castellano et al. (2022) for the $z \sim 10$ galaxies, based on B23, all in the low-μ regime ($\mu < 3.8$), are well in agreement with the values computed with the new lens model.

An additional way to demonstrate the robustness of the lens model is to compare the model-predicted redshift values of the nonspectroscopic systems with the photometric redshift estimates for their multiple images. In Figure 10, we show a comparison between the probability density distributions of the redshift values obtained from the EM lens model (gray histogram) and the photometric redshift estimated by exploiting the JWST and HST multiband data (see Section 2.1) as the colored histograms, for the six nonspectroscopic multiple-image systems included in the lens model. The remaining two nonspectroscopic systems (i.e., Sys-301 and Sys-200) used in the model do not have reliable photometric redshift measurements for any of their images, due to their faintness and to light contamination from nearby objects and, for that reason, are not included in the figure. The photometric Sys-7, Sys-28, and Sys-53 are located in the main cluster field (around the cluster BCGs) and have three multiple images each, corresponding to the nine red circles in Figure 5. From the JWST and HST

multiband observations, we obtain consistent photometric redshift estimates for two out of the three multiple images of Sys-7 and Sys-28 (i.e., 7a, 7c, 28a, and 28b). While for Sys-28 the photometric redshifts are in very good agreement with the EM predicted redshift, we find that the model-predicted redshift of Sys-7 is underestimated compared to the photometric estimates. Regarding Sys-53, the photometric redshift probability distribution for image 53b peaks at $z_{\rm ph}^{\rm peak}(53b) = 1.575$, which is well below the photometric redshift values inferred for the other two multiple images, 53a and 53c (yellow and green histograms in the plot, respectively) and the model-predicted redshift. The likely reason for this discrepancy is the light contamination produced by a cluster galaxy (with $m_{\rm F160W} = 22.05$) residing at a projected distance of just $0\farcs9$ from the image 53b. Moreover, Furtak et al. (2022) have measured a photometric redshift of $z_{\rm ph}(\text{Sys-53}) \sim 7.7$, in very good agreement with our model-predicted redshift and with the photometric redshifts of the images 53a and 53c from this work. Sys-601 and Sys-602 both reside around the bright galaxy G2 and count three and four multiple images, respectively (these correspond to the seven green circles around galaxy G2 in Figure 5; see also the dashed white squares in Figure 6). The multiband photometric data allow for the estimate of the photometric redshifts for all the multiple images of the systems. These are found to be compatible among each other and with the lens model-predicted redshift probability density distributions. We note that we obtain identical redshift values for the two systems. Considering that the Sys-601 and Sys-602 sources are just $2\farcs1$ apart (corresponding to 17.5 kpc at $z = 2.3$), we can argue that these are likely two galaxies belonging to the same gravitationally bound system. We also note that the positions of the images of the Sys-601 and Sys-602 are extremely well reproduced by the EM with values of $\Delta_{\rm rms}^{\rm Sys-601} = 0\farcs28$ and $\Delta_{\rm rms}^{\rm Sys-601} = 0\farcs22$. Finally, Sys-700 consists of three multiple images forming around galaxy G3 (blue circles in Figure 5). Also in this case, the lens model-predicted redshift is in very good agreement with the photometric redshift estimated for the single image 700.1c.

5. Conclusions

We have presented a new high-precision strong-lensing model of the galaxy cluster A2744 ($z = 0.3072$) based on the deep, wide-field JWST/NIRCam imaging (Bezanson et al. 2022; Treu et al. 2022; Paris et al. 2023) and new MUSE DDT observations, together with extensive archival spectrophotometric data sets including two recent spectroscopic redshifts with JWST/NIRISS and JWST/NIRSpec (Roberts-Borsani et al. 2023; Vanzella et al. 2022; Lin et al. 2023). The model is constrained by 149 multiple images (121 of which are spectroscopically confirmed) from 50 background sources, spanning a very wide redshift range between 1.03 and 9.76. The multiple-image catalog compiled for this cluster is the largest to date (see Figure 4) and represents an increase of about 66% with respect to our previous, HST-based lens model (B23). Specifically, we have included 27 additional multiple images in the main cluster core (18 of which are spectroscopically confirmed) thanks to a reanalysis of faint multiple images in the archival MUSE and the JWST/NIRISS data. In addition, the deep, high-resolution JWST/NIRCam observations have proved to be key in the identification of a large number of multiple-image systems around the external clumps, in particular those associated with the bright galaxies G1 and G2 (see also F23), where we have considered 29 multiple images from 10 background sources. By analyzing the new data from the MUSE DDT program, we have presented the first spectroscopic redshift of a multiple-image system in the G1–G2 external clump, a face-on spiral galaxy at $z = 2.584$.

The model includes 177 cluster member galaxies, 163 of which are spectroscopically confirmed (24 of them are newly confirmed with the new MUSE data), and 14 are securely identified as cluster members with a CNN deep-learning technique (Angora et al. 2020). The new subhalo scaling relation is consistent, within the 1σ statistical uncertainties, with the measured one shown by B23, demonstrating the accurate total mass modeling of the lens cluster.

The total rms separation between the observed and model-predicted positions of the 149 multiple images is $\Delta_{\rm rms}^{\rm TOT} = 0\farcs43$ on the image plane (see Figure 7). The achieved precision is similar to that obtained by B23 ($\Delta_{\rm rms}^{\rm TOT} = 0\farcs37$), despite the significantly larger number of multiple images considered in this work. We note that the precision of our model is significantly better than that of the JWST-based lens model presented by F23, who quote a $\Delta_{\rm rms}^{\rm TOT} = 0\farcs66$ on the lens plane. The newly included multiple-image systems around the external clumps represent a leap forward in the lens modeling of A2744 in terms of precision and accuracy. While the cumulative projected total mass profiles and the magnification maps obtained from our new model are highly consistent with those obtained by B23 in the main cluster core, these quantities are robustly reconstructed at larger radii with significantly smaller statistical uncertainties (see Figures 8 and 9) thanks to the newly included constraints. The robustness of the lens model is further demonstrated by the consistency between the model-predicted and photometric redshift estimates of six nonspectroscopic multiple-image systems included in the model (see Figure 10).

Our new lens model holds a fundamental role in the study of the lensed high-redshift sources that are being observed by the JWST in this cluster field (e.g., Castellano et al. 2022; Morishita et al. 2023; Prieto-Lyon et al. 2023), in particular in the high-magnification regime (e.g., Roberts-Borsani et al. 2023; Vanzella et al. 2022). Further improvements will be possible when additional multiple-image systems will be spectroscopically confirmed with ongoing JWST spectroscopic observations.

The lens model presented in this work will be made publicly available with the publication of this paper through our recently developed Strong Lensing Online Tool (`SLOT`; B23), allowing researchers to take full advantage of the predictive and statistical results of our lens model through a user-friendly graphical interface. The complete catalog of secure redshift measurements (i.e., QF $\geqslant$2) from the new VLT/MUSE DDT observations (see Section 2.2) will also be released upon publication.

Acknowledgments

The authors thank the anonymous referee for helpful comments which improved the manuscript. Support for program JWST ERS-1324 was provided by NASA through a grant from the Space Telescope Science Institute, which is operated by the Association of Universities for Research in

Astronomy, Inc., under NASA contract NAS 5-03127. The Hubble Frontier Field program (HFF) and the Beyond Ultra-deep Frontier Fields And Legacy Observations (BUFFALO) are based on the data made with the NASA/ESA Hubble Space Telescope. The Space Telescope Science Institute is operated by the Association of Universities for Research in Astronomy, Inc., under NASA contract NAS 5-26555. ACS was developed under NASA Contract NAS 5-32864. Based also on observations collected at the European Southern Observatory for Astronomical research in the Southern Hemisphere under ESO programs with IDs 094.A-0115 (PI: Richard). We acknowledge financial support through grant Nos. PRIN-MIUR 2015W7KAWC, 2017WSCC32, and 2020SKSTHZ. A.A. has received funding from the European Union's Horizon 2020 research and innovation program under the Marie Skłodowska-Curie grant agreement No. 101024195ROSEAU. G.B.C. thanks the Max Planck Society for support through the Max Planck Research Group for S. H. Suyu and the academic support from the German Centre for Cosmological Lensing. M. M. acknowledges support from the Italian Space Agency (ASI) through contract "Euclid—Phase D." We acknowledge funding from the INAF "main-stream" grant Nos. 1.05.01.86.20 and 1.05.01.86.31. We acknowledge support from the INAF Large Grant 2022 "Extragalactic Surveys with JWST" (PI: Pentericci). This research is supported in part by the Australian Research Council Centre of Excellence for All Sky Astrophysics in 3 Dimensions (ASTRO 3D), through project No. CE170100013. The GLASS-JWST data are associated with doi:10.17909/mrt6-wm89 (NIRCam) and doi:10.17909/9a2g-sj78 (NIRSpec). The UNCOVER NIRcam data are associated with doi:10.17909/zn4s-0243. The JWST data from the DDT program 2756 are associated with doi:10.17909/te6f-cg91.

Facilities: JWST(NIRCam), JWST(NIRISS), VLT(MUSE), HST(ACS), HST(WFC3).

Appendix A
Catalog of Multiple Images in A2744

We present in Table 2 the complete catalog of multiple images included in the new lens model in the JWST WCS (see Section 2.1). For consistency, we also list the multiple images presented in the B23 HST-based lens model (marked with a dagger symbol, †) that were anchored to the HFF WCS. The multiple images identified with a star symbol (⋆) indicate those newly spectroscopically confirmed with the central MUSE data cube, while those with an asterisk (*) have been spectroscopically confirmed with JWST/NIRISS (Vanzella et al. 2022; Lin et al. 2023) and JWST/NIRSpec (Roberts-Borsani et al. 2023). Further details can be found in B23 and in Section 3.2.

Table 2
List of the Multiple Images Used as Constraints in the `Extended Model` We Are Presenting

ID	R.A. (deg)	Decl. (deg)	QP	z	QF	Location
1.1a†	3.597551	−30.403906	1	1.688	3	BGCs
1.1b†	3.595952	−30.406787	1	1.688	2	BGCs
1.1c†	3.586210	−30.409963	1	1.688	3	BGCs
600.5a	3.542933	−30.367952	1	2.580	2	G1–G2
600.5b	3.540186	−30.372640	1	2.580	2	G1–G2
600.5c	3.540297	−30.374845	1	2.580	2	G1–G2
…	…	…	…	…	…	…

Notes. The multiple images of the same background source share the same numerical part of the ID (first column). In the fourth column, we quote the redshifts of the sources. The "positional quality flag," QP, quantifies the precision in determining the on-sky position of the multiple images. QP = 1 corresponds to images with a compact HST or JWST emission. The positional error assumed on these images in the lens model is the lowest. QP = 2 stands for a diffuse or elongated HST or JWST emission. An intermediate positional error is associated to these images. Images with QP = 3 are only detected in the MUSE data cube or are characterized by a very diffuse emission. These have the largest positional errors. In the last column, we report the region of the cluster where the multiple images are located. These regions are identified using the name of the brightest galaxies they contain (see Figure 5). The catalog is published in its entirety in the machine-readable format. A portion is shown here for guidance regarding its form and content.

(This table is available in its entirety in machine-readable form.)

Appendix B
Redshift Catalog

In Table 3, we present the complete catalog of all the sources for which we measure a secure redshift value (QF $\geqslant$2) from the new MUSE data obtained during the ESO DDT program

Table 3
Full Catalog of the Sources with a Reliable Redshift Measurement from the VLT/MUSE Data Obtained During the ESO DDT Program 109.24EZ.001

ID	R.A. (deg)	Decl. (deg)	z	QF
70004500	3.489919	−30.323177	0.273	3
70001493	3.531806	−30.359859	0.297	3
70005157	3.497156	−30.318811	0.3430	3
70004656†	3.491547	−30.325847	1.3762	3
70003446†	3.483330	−30.332151	5.0664	3
…	…	…	…	…

Notes. The values of the QF are described in Section 2.2. The catalog is published in its entirety in the machine-readable format. A portion is shown here for guidance regarding its form and content.

(This table is available in its entirety in machine-readable form.)

109.24EZ.001 (see Section 2.2 and Figure 1). The foreground, cluster member, and background galaxies are listed in the top, middle, and bottom panels of Table 3, respectively. The 42 UV-faint galaxies at $z \sim 3$–7 published by Prieto-Lyon et al. (2023) are identified with a dagger symbol (†) in the ID.

ORCID iDs

Pietro Bergamini https://orcid.org/0000-0003-1383-9414
Ana Acebron https://orcid.org/0000-0003-3108-9039
Claudio Grillo https://orcid.org/0000-0002-5926-7143
Piero Rosati https://orcid.org/0000-0002-6813-0632
Gabriel Bartosch Caminha https://orcid.org/0000-0001-6052-3274
Amata Mercurio https://orcid.org/0000-0001-9261-7849
Eros Vanzella https://orcid.org/0000-0002-5057-135X
Charlotte Mason https://orcid.org/0000-0002-3407-1785
Tommaso Treu https://orcid.org/0000-0002-8460-0390
Giuseppe Angora https://orcid.org/0000-0002-0316-6562
Gabriel B. Brammer https://orcid.org/0000-0003-2680-005X
Massimo Meneghetti https://orcid.org/0000-0003-1225-7084
Mario Nonino https://orcid.org/0000-0001-6342-9662
Kristan Boyett https://orcid.org/0000-0003-4109-304X
Maruša Bradač https://orcid.org/0000-0001-5984-0395
Marco Castellano https://orcid.org/0000-0001-9875-8263
Adriano Fontana https://orcid.org/0000-0003-3820-2823
Takahiro Morishita https://orcid.org/0000-0002-8512-1404
Diego Paris https://orcid.org/0000-0002-7409-8114
Gonzalo Prieto-Lyon https://orcid.org/0000-0003-3518-0374
Guido Roberts-Borsani https://orcid.org/0000-0002-4140-1367
Namrata Roy https://orcid.org/0000-0002-4430-8846
Paola Santini https://orcid.org/0000-0002-9334-8705
Benedetta Vulcani https://orcid.org/0000-0003-0980-1499
Xin Wang https://orcid.org/0000-0002-9373-3865
Lilan Yang https://orcid.org/0000-0002-8434-880X

References

Adams, N. J., Conselice, C. J., Ferreira, L., et al. 2023, MNRAS, 518, 4755
Angora, G., Rosati, P., Brescia, M., et al. 2020, A&A, 643, A177
Bacon, R., Accardo, M., Adjali, L., et al. 2012, Msngr, 147, 4
Balestra, I., Mercurio, A., Sartoris, B., et al. 2016, ApJS, 224, 33
Bender, R., Burstein, D., & Faber, S. M. 1992, ApJ, 399, 462
Bergamini, P., Acebron, A., Grillo, C., et al. 2023a, A&A, 670, A60
Bergamini, P., Grillo, C., Rosati, P., et al. 2023b, A&A, 674, A79
Bergamini, P., Rosati, P., Mercurio, A., et al. 2019, A&A, 631, A130
Bezanson, R., Labbe, I., Whitaker, K. E., et al. 2022, arXiv:2212.04026
Bouwens, R. J., Illingworth, G. D., van Dokkum, P. G., et al. 2021, AJ, 162, 255
Bradley, L. D., Coe, D., Brammer, G., et al. 2022, arXiv:2210.01777
Braglia, F. G., Pierini, D., Biviano, A., & Boehringer, H. 2009, A&A, 500, 947
Bruzual, G., & Charlot, S. 2003, MNRAS, 344, 1000
Caminha, G. B., Grillo, C., Rosati, P., et al. 2017a, A&A, 600, A90
Caminha, G. B., Grillo, C., Rosati, P., et al. 2017b, A&A, 607, A93
Caminha, G. B., Rosati, P., Grillo, C., et al. 2019, A&A, 632, A36
Caminha, G. B., Suyu, S. H., Mercurio, A., et al. 2022, A&A, 666, L9
Castellano, M., Fontana, A., Treu, T., et al. 2022, ApJL, 938, L15
Castellano, M., Sommariva, V., Fontana, A., et al. 2014, A&A, 566, A19
Chen, W., Kelly, P. L., Treu, T., et al. 2022, ApJL, 940, L54
Diego, J. M., Pascale, M., Kavanagh, B. J., et al. 2022, A&A, 665, A134
Elíasdóttir, Á., Limousin, M., Richard, J., et al. 2007, arXiv:0710.5636
Faber, S. M., Dressler, A., Davies, R. L., et al. 1987, in Nearly Normal Galaxies. From the Planck Time to the Present, ed. S. M. Faber (New York: Springer-Verlag), 175
Fontana, A., D'Odorico, S., Poli, F., et al. 2000, AJ, 120, 2206
Furtak, L. J., Zitrin, A., Plat, A., et al. 2022, arXiv:2212.10531
Furtak, L. J., Zitrin, A., Weaver, J. R., et al. 2023, MNRAS, 523, 4568
Grillo, C., Karman, W., Suyu, S. H., et al. 2016, ApJ, 822, 78
Hsiao, T. Y.-Y., Coe, D., & Abdurro'uf 2023, ApJL, 949, L34
Jullo, E., & Kneib, J.-P. 2009, MNRAS, 395, 1319
Jullo, E., Kneib, J.-P., Limousin, M., et al. 2007, NJPh, 9, 447
Kelly, P. L., Diego, J. M., Rodney, S., et al. 2018, NatAs, 2, 334
Kneib, J.-P., Ellis, R. S., Smail, I., Couch, W. J., & Sharples, R. M. 1996, ApJ, 471, 643
Limousin, M., Kneib, J.-P., & Natarajan, P. 2005, MNRAS, 356, 309
Lin, X., Cai, Z., Zou, S., et al. 2023, ApJL, 944, L59
Lotz, J. M., Koekemoer, A., Coe, D., et al. 2017, ApJ, 837, 97
Mahler, G., Jauzac, M., Richard, J., et al. 2023, ApJ, 945, 49
Mahler, G., Richard, J., Clément, B., et al. 2018, MNRAS, 473, 663
Meena, A. K., Zitrin, A., Jiménez-Teja, Y., et al. 2023, ApJL, 944, L6
Meneghetti, M., Natarajan, P., Coe, D., et al. 2017, MNRAS, 472, 3177
Merlin, E., Bonchi, A., Paris, D., et al. 2022, ApJL, 938, L14
Merlin, E., Castellano, M., Santini, P., et al. 2021, A&A, 649, A22
Merten, J., Coe, D., Dupke, R., et al. 2011, MNRAS, 417, 333
Meštrić, U., Vanzella, E., Zanella, A., et al. 2022, MNRAS, 516, 3532
Morishita, T., Roberts-Borsani, G., Treu, T., et al. 2023, ApJL, 947, L24
Owers, M. S., Randall, S. W., Nulsen, P. E. J., et al. 2011, ApJ, 728, 27
Paris, D., Merlin, E., Fontana, A., et al. 2023, arXiv:2301.02179
Pascale, M., Frye, B. L., Diego, J., et al. 2022, ApJL, 938, L6
Prieto-Lyon, G., Strait, V., Mason, C. A., et al. 2023, A&A, 672, A186
Priewe, J., Williams, L. L. R., Liesenborgs, J., Coe, D., & Rodney, S. A. 2017, MNRAS, 465, 1030
Raney, C. A., Keeton, C. R., & Zimmerman, D. T. 2021, MNRAS, 508, 5587
Richard, J., Claeyssens, A., Lagattuta, D., et al. 2021, A&A, 646, A83
Roberts-Borsani, G., Morishita, T., Treu, T., et al. 2022, ApJL, 938, L13
Roberts-Borsani, G., Treu, T., Chen, W., et al. 2023, Natur, 618, 480
Santini, P., Fontana, A., Castellano, M., et al. 2023, ApJL, 942, L27
Schaerer, D., & de Barros, S. 2009, A&A, 502, 423
Schmidt, K. B., Treu, T., Brammer, G. B., et al. 2014, ApJL, 782, L36
Soto, K. T., Lilly, S. J., Bacon, R., Richard, J., & Conseil, S. 2016, MNRAS, 458, 3210
Steinhardt, C. L., Jauzac, M., Acebron, A., et al. 2020, ApJS, 247, 64
Talia, M., Mignoli, M., Cimatti, A., et al. 2012, A&A, 539, A61
Treu, T., Roberts-Borsani, G., Bradac, M., et al. 2022, ApJ, 935, 110
Treu, T., Schmidt, K. B., Brammer, G. B., et al. 2015, ApJ, 812, 114
Vanzella, E., Castellano, M., Bergamini, P., et al. 2022, A&A, 659, A2
Vanzella, E., Claeyssens, A., Welch, B., et al. 2023, ApJ, 945, 53
Vulcani, B., Treu, T., Calabro, A., et al. 2023, ApJL, 948, L15
Wang, X., Hoag, A. T., Huang, K.-H., et al. 2015, ApJ, 811, 29
Weilbacher, P. M., Palsa, R., Streicher, O., et al. 2020, A&A, 641, A28
Welch, B., Coe, D., Zackrisson, E., et al. 2022, ApJL, 940, L1
Welch, B., Coe, D., Zitrin, A., et al. 2023, ApJ, 943, 2
Williams, H., Kelly, P. L., Chen, W., et al. 2023, Sci, 380, 416
Willott, C. J., Doyon, R., Albert, L., et al. 2022, PASP, 134, 025002
Windhorst, R. A., Cohen, S. H., Jansen, R. A., et al. 2023, AJ, 165, 13
Zitrin, A., Zheng, W., Broadhurst, T., et al. 2014, ApJL, 793, L12